

Exploring the Influence of Linker Substitution and Ratios on Cooperative Framework Flexibility Through the Mixed-Linker Approach

Arijit Halder and C. Michael McGuirk*

Department of Chemistry, Colorado School of Mines, Golden, Colorado 80401, United States

Abstract

Cooperatively flexible metal–organic frameworks that exhibit step-shaped, or Type V-like, adsorption–desorption profiles can lower requisite pressure–temperature swings, thus energy input, necessary for an array of gas storage, delivery, and separations applications. However, such benefits are lost if the pressure threshold of the adsorption and desorption steps at a given temperature do not match the conditions dictated by the application, such as H₂ storage and delivery or olefin–paraffin separations. Unfortunately, the discovery of cooperatively flexible frameworks remains wholly serendipitous, and *de novo* design remains impossible. Accordingly, there is great need to further our understanding of flexibility such that we can intuitively derivatize known frameworks and, ultimately, design entirely new ones to meet the requisite conditions of energy consumptive processes. In this work, we demonstrate that the mixed-linker, or multivariate, approach is a powerful tool for the derivation of a known flexible framework, with variances in linker substitution and ratio giving rise to a family wherein significant changes to the step-shaped adsorption–desorption profiles for multiple adsorbates are observed. Specifically, we report twelve isostructural mixed-linker derivatives of CdIF-13 (*sod*-Cd(benzimidazolate)₂) with six point-modified benzimidazole linkers spontaneously synthesized through prototypical solvothermal conditions. Each is shown by PXRD to exhibit similar reversible flexibility to CdIF-13, and by TGA and DSC to be similarly thermally stable. Isothermal gas adsorption measurements with N₂ at 77 K, CO₂ at 195 K, and propane at 298 K demonstrate the wide ranging, adsorbate-dependent effects of linker substitution and ratio, including dramatic reductions in the adsorption threshold

pressure, evolution of multiple steps, and complete absence of observable adsorption. Aided by prior crystallographic characterization of CdIF-13, the observed trends are analyzed in an attempt to resolve the influence of linker substitution and ratios on behavior. In total, this work illustrates how the mixed-linker approach enables the synthesis and study of a large catalog of functionally modified frameworks, which can help identify the variables that influence flexibility and sorption behavior.

1. Introduction

Metal–organic frameworks are a broad class of permanently porous, three-dimensionally connected crystalline lattices, composed of inorganic nodes connected by polytopic organic linkers.¹ The high structural and chemical modularity of these frameworks enables intuitive synthetic access to crystalline architectures with an unparalleled diversity of pore structure and surface chemistry,^{2,3} which has been expansively tuned for applications in gas storage,^{3,4} chemical separation,^{5,6} chemical sensors,⁷ heterogeneous catalysis,^{8,9} and, more recently, light-harvesting^{10,11} and electron conductivity.^{12,13} While a great variety exists, most frameworks are macroscopically rigid, with continuous pore structures across relevant temperatures, adsorbate pressure, and mechanical pressure conditions.^{14,15} Yet, the apparent ubiquity of localized dynamics under relevant conditions, including linker rotation and dissociation, has been more recently recognized. Indeed, these local dynamics, existing as shallow energetic variations of the long-range structure, can have significant, though transient, impacts on pore size, shape, and chemistry, thus observable properties.¹⁶⁻¹⁹ However, these local dynamics are largely uncontrolled, existing under equilibrium owing to the low energy barriers between accessible states.^{17,18} This begs the question of the functional implications of there being large, yet traversable, kinetic barriers between multiple accessible and isolatable states of varying pore size, shape, and chemistry.

There exists a small subclass of metal–organic frameworks that exhibit periodic, or cooperative, reversible topological changes in response to external stimuli, such as varying adsorbate pressure and temperature.^{14, 15, 20} Whereas rigid frameworks retain the as-synthesized structure upon solvent removal (i.e., activation),^{14, 15, 20} these cooperatively flexible (i.e., soft or dynamic) frameworks, undergo a phase change upon activation to a typically denser phase through appreciable changes to symmetry and pore architecture, with little-to-no changes in network connectivity.^{15, 20} This denser phase is typically thermodynamically more stable in the absence of adsorbates, owing to an increase in exothermic inter-linker contacts.²⁰ A return to the as-synthesized phase, or close to it, can be typically triggered through an absorption event that enthalpically stabilizes the less dense form.^{20, 21} These cooperative phase changes take many forms, but most often occur through skeletal distortion, linker rotation, displacement of lattice components, or some combination of the three.²² In contrast to local dynamics, these long-range cooperative event occur in the first order manner (i.e., discontinuous), owing to appreciable energy barriers between the structural states. Thus, the different states are kinetically stable under specific pressure–temperature conditions and can be discretely isolated and characterized.^{20, 21, 23}

Cooperatively flexible frameworks typically exhibit divergent adsorption–desorption behavior from rigid counterparts, which most often have Type I Langmuir profiles (**Figure 1a**).²⁴ Where cooperative flexibility occurs in a first order fashion and results in substantial changes to the accessible porosity, switching between a low(er) porosity “closed” phase and a high(er) porosity “open” phase, the frameworks can exhibit Type V-like, or step-shaped, isothermal adsorption–desorption profiles (**Figure 1b**).^{23, 24}

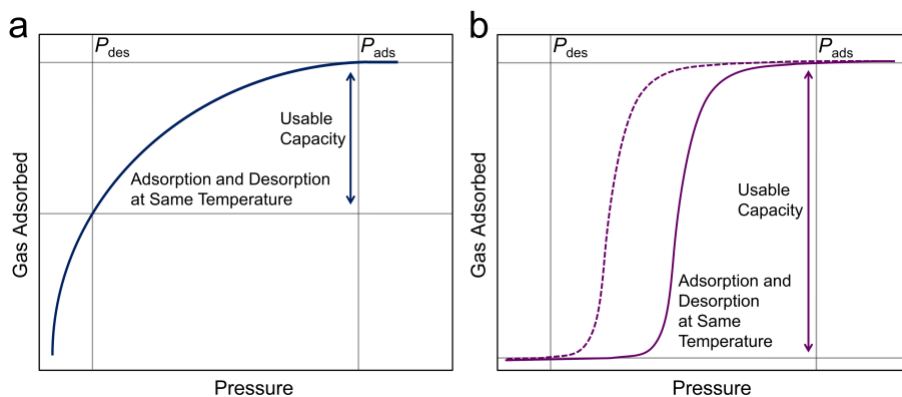


Figure 1. (a) Rigid frameworks typically exhibit a type I Langmuir adsorption-desorption profile. Materials with this adsorption-desorption profile require large changes in pressure and/or temperature to uptake and deliver their gaseous payload. Thus, under application-relevant conditions, the usable capacity is much lower than the total storage capacity. (b) Step-shaped adsorption-desorption profiles (i.e., Type V-like), often exhibited by cooperatively flexible frameworks, can enable usable capacities approaching the total uptake capacity, often with reduced pressure and/or temperature swing inputs. Here maximum adsorption pressure (P_{ads}) and minimum desorption pressure (P_{des}) are presented by vertical lines and the deliverable capacities are indicated by double headed arrow.

Depending on the kinetic stability of the adsorbate-saturated open phase, desorption upon lowering adsorbate pressure can occur in a Type I or V-like fashion, typically with some hysteresis.²⁴ If both adsorption and desorption occur in a step-shaped fashion, low-energy storage, transport, and delivery of gaseous payloads is possible due the reduced requisite swings in pressure and/or temperature relative to those necessitated by porous materials with Type I profiles.²⁵⁻²⁷

Despite these advantages, there is a core issue.^{25, 26} As a field, we have little understanding of the structural and/or energetic origins of cooperative flexibility, and the discovery of frameworks with step-shaped adsorption-desorption is entirely serendipitous. In contrast to the now routine design of rigid frameworks for specific applications from constituent linkers and nodes,^{2-4, 28, 29} there is no ability to do so with flexible frameworks. Thus, if step-shaped adsorption-desorption

does not occur in the necessary pressure–temperature regime for a given storage and delivery application the benefit is lost. Accordingly, there are two related needs to advance the understanding and utility of cooperatively flexible frameworks: (i) The ability to intuitively and precisely derivatize known frameworks to meet the functional needs of specific applications, and (ii) The advancement of fundamental understanding of cooperative flexibility towards enabling *de novo* design.

Significant efforts have been made in the derivatization of known flexible frameworks through substitution of the inorganic node species and/or functionalization of organic linkers, producing insights into variables that influence phase stability and flexibility.³⁰⁻³² For example, wholesale linker functionalization of Co(bdp), such as fluorination and methylation, shifts the adsorption threshold pressure without dramatically affected the overall shape of the stepped adsorption profile.^{26,30} Our own studies have focused on ZIF-7 (*sod*-Zn(benzimidazolate)₂), which we recently characterized through *in situ* neutron powder diffraction experiments to undergo a first order phase change through combined skeletal distortion and linker rotation,³³ wherein the low porosity closed phase is stabilized by inter-linker C–H \cdots π and $\pi\cdots\pi$ interactions (**Figure S1**). By switching out Zn(II) for Cd(II) to form CdIF-13 (*sod*-Cd(benzimidazolate)₂) (**Figure 2, S2**), we found that this congener exhibited a dramatic changes to the total capacity, pre-step adsorption, and adsorption threshold pressures.³⁴ Characterization of the closed phase by single-crystal X-ray diffraction suggested that the latter two features result from closer inter-linker C–H \cdots π and $\pi\cdots\pi$ interactions (**Figure 3**).³³ However, for many relevant adsorbates, such as H₂, the adsorption threshold pressure of CdIF-13 is prohibitively high,²⁵ apparently due to these stronger inter-linker interactions creating a larger energy barrier for adsorption-induced framework opening.

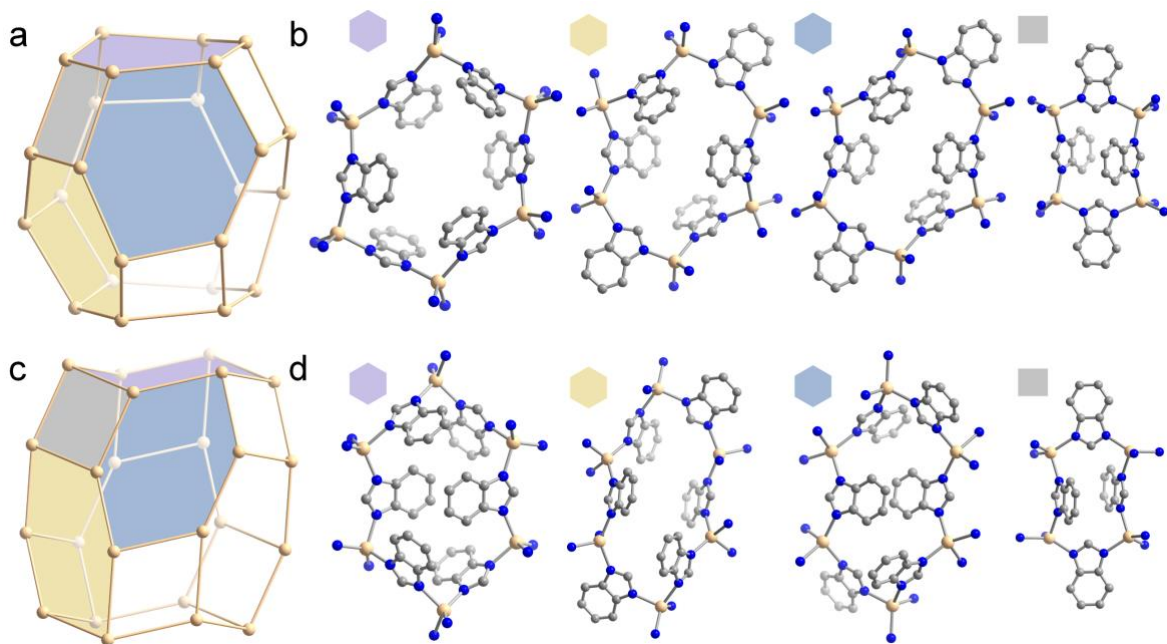


Figure 2. (a) Discrete sodalite cage of the *N,N*-dimethylformamide (DMF)-solvated CdIF-13 (adapted from ref 34), as determined by single-crystal X-ray diffraction, composed of six- and four-membered rings represented by different colored polygons. The beige colored lines represent benzimidazolate (bim⁻) linkers which connect two tetrahedral Cd(II) nodes denoted by beige spheres. (b) Structures of the distinct six- and four-membered rings within the individual sodalite cage, as determined by single-crystal X-ray diffraction, with their respective locations color-coded according to (a). Solvent has been excluded for clarity. (c) Individual sodalite cage of the activated CdIF-13 (adapted from ref 33), as determined by single-crystal X-ray diffraction, created by different six- and four-membered rings presented by different colored polygons. (d) Representation of the different six- and four-membered rings present in the sodalite cage, as determined by single-crystal X-ray diffraction with their individual locations color-coded according to (c). Grey, dark blue and beige, spheres represent C, N, and Cd, respectively; hydrogen atoms are omitted for clarity.

Therefore, we sought to modulate CdIF-13 in a manner that would dramatically lower this threshold through the recently developed mixed-linker, or multivariate, approach to framework derivatization.³⁵ In this approach two or more related linkers, such as benzimidazole and 5-fluorobenzimidazole, are in solution during solvothermal synthesis (**Figure 4a**) and are spontaneously incorporated into the framework lattice as a random solid-state solution. By controlling the ratio of linkers in the synthesis mixture, the ratio incorporated into the framework

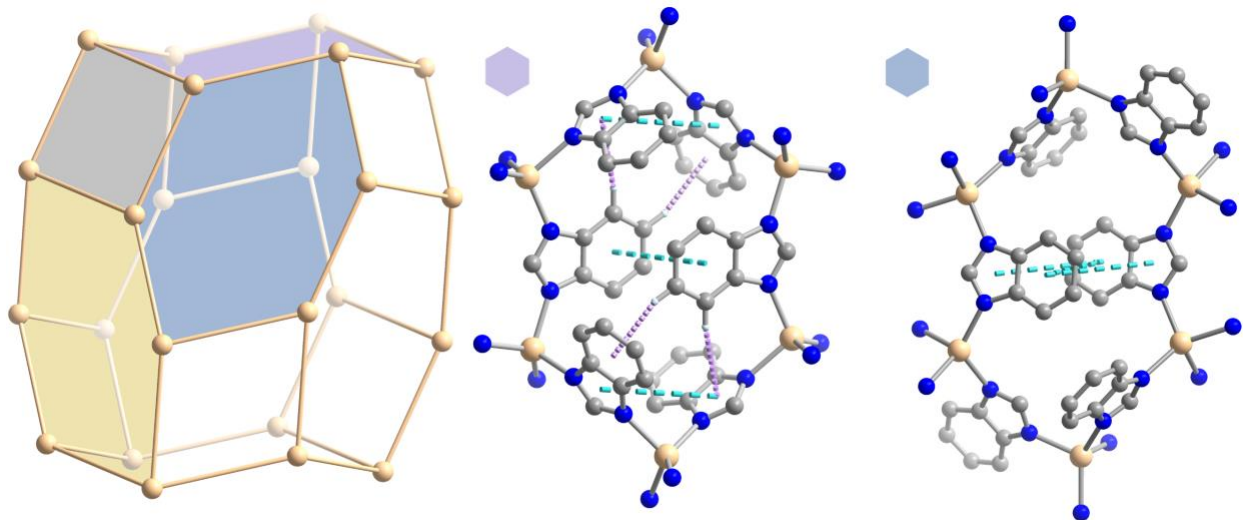


Figure 3. (Left) Structural constituent of activated CdIF-13 (adapted from ref 33), as determined by single-crystal X-ray diffraction, created by different six- and four-membered rings presented by different colored polygons. Whereas rest of the figures presents different intramolecular weak interactions, $\pi \cdots \pi$ interactions (cyan dashed lines) (distance $< 4.7 \text{ \AA}$ and dihedral angle $< 15^\circ$) and C–H $\cdots\pi$ interactions (magenta dashed lines) (hydrogen to center of ring distance $< 3 \text{ \AA}$) present in the individual six-membered rings of activated CdIF-13. Grey, dark blue and beige, spheres represent C, N, and Cd, respectively; the hydrogen atoms involved in C–H $\cdots\pi$ bond are presented with sky blue colored spheres whereas rest of the hydrogen atoms are omitted for clarity. Yellow ring is not presented here due to lack of any $\pi \cdots \pi$ and C–H $\cdots\pi$ interactions in the mentioned distance-angle range.

can be altered. We found that by using this mixed-linker approach with benzimidazole and 2-methyl-5,6-difluorobenzimidazole (2M56DFbim) the flexibility and adsorption threshold could be dramatically altered by the apparent influence of fluorination on the inter-linker interactions thought to stabilize the closed phase.³⁶ Excitingly, with the 14:1 framework (*sod*-Cd(bim)_{1.87}(2M56DFbim)_{0.13}) step-shaped adsorption-desorption of weakly adsorbing H₂ could be observed at 77 and 87 K below 100 bar.²⁵ Which, owing to the adsorption threshold pressures and narrow desorption hysteresis, enables large working capacities with relatively small swings in pressure, as well as the ability to deliver the payload at high pressures, obviating costly repressurization.²⁵

Encouraged by these results (**Figure 2**), we herein sought to more broadly explore the mixed-linker approach in a cooperatively flexible framework. In this work, we report 12 isorecticular mixed-linker derivatives of CdIF-13, combining benzimidazole with six substituted linker derivatives. These 12 frameworks consist of three series of three frameworks with the linkers 5-fluoro-, 5,6-difluoro-, and 5-methylbenzimidazole, two frameworks at a ratio of ~3:1 with 5-chloro- and 5-bromo-benzimidazole, and the last framework at the lowest observable ratio with 5-cyanobenzimidazole. These 12 have been selected from a larger catalog of approximately 50 that have been synthesized and characterized in our lab, which we note to emphasize the power of the mixed-linker approach for derivatization of known flexible frameworks. Through powder X-ray diffraction (PXRD) measurements and isothermal adsorption measurements with three different probe gasses (N₂ at 77 K, CO₂ at 195 K, and propane at 298 K) we have characterized the influence of these different substitutions at varying ratios. In combination with previous structural characterization of CdIF-13, we can begin to infer key variables that influence step-shaped adsorption–desorption behavior, towards targeted derivatization, advanced fundamental understanding, and *de novo* design.

2. Experimental Methods

2.1. General Procedures

All reagents and solvents were obtained from commercial sources, with a purity level of 95% or higher. These materials were used as received, without further purification. Benzimidazole (98%), 5-methylbenzimidazole (96%) and 5-chlorobenzimidazole (96%) were procured from Sigma–Aldrich. 5-bromobenzimidazole (97%) was purchased from Oakwood Chemical. 5-fluorobenzimidazole (98%) was purchased from Ambeed. 5,6-difluorobenzimidazole (95%) and 5-cyanobenzimidazole (95%) were purchased from Enamine. Cadmium perchlorate hydrate was

obtained from Strem Chemicals. Ultrahigh purity (99.999%) He, N₂, and propane, and industrial purity grade CO₂ (99.95%) were purchased from General Air and used for all adsorption experiments. Dichloromethane (DCM) and *N,N*-dimethylformamide (DMF) were acquired from Fisher Scientific.

2.2. Synthesis

2.2.1. Synthesis and Activation of CdIF-13

The base material, CdIF-13 was synthesized following a previously reported procedure. Please note, for synthesis, Cd(ClO₄)₂·xH₂O is used as the cadmium source, which is an oxidant and acutely toxic. This chemical should be used with necessary precautions.

Cd(ClO₄)₂·xH₂O (300 mg), benzimidazole (118 mg, 1 mmol) and 2 mL of *N,N*-dimethylformamide (DMF) were added to a 4 mL vial, and closed with Teflon lined cap. This is then sonicated until all solids were dissolved and then placed in an oven at 130 °C for 24 h. After 24h, the reaction mixture was allowed to cool to room temperature naturally by shutting off the oven. The resulting colorless crystals of CdIF-13 were collected via vacuum filtration and washed with excess DMF to remove any unreacted materials. Adsorbed DMF molecules were removed by solvent exchange with dichloromethane (DCM). At first, the product was thoroughly washed with DCM and then it is kept in 15 mL DCM for 24h. After 24h, the resulting white polycrystalline powder was collected by filtration and washed again with DCM (50 mL). Finally, the powder was activated at 150 °C under dynamic vacuum for 24 h. The *sod* topology and phase change upon activation were confirmed by PXRD measurements (**Figure S3**). The removal of all solvent upon activation was confirmed by ¹H NMR spectroscopy in DMSO-*d*₆ (**Figure S17**).

2.2.2. Synthesis and Activation of Mixed-Linker Frameworks.

The above synthetic approach for CdIF-13 was adapted for the mixed-linker frameworks to include the presence of the second linker. Specifically, a substituted benzimidazole was included in the synthesis solution in different ratios to the baseline benzimidazole as presented in **Table 1**, maintaining the total linker amount as 1 mmol (equimolar to $\text{Cd}(\text{ClO}_4)_2 \cdot x\text{H}_2\text{O}$, 1 mmol). In general, $\text{Cd}(\text{ClO}_4)_2 \cdot x\text{H}_2\text{O}$ (310 mg), benzimidazole, the second linker, and 2 mL of *N,N*-dimethylformamide (DMF) were charged in a 4 mL scintillation vial, closed with a Teflon sealed cap, and sonicated until all solids were dissolved. The vial was then placed in an oven at 130 °C for a certain number of days as mentioned in **Table 1**. After completion, as visually determined by the presence of a static amount of solid product in the reaction vial, the reaction mixture was allowed to cool to room temperature naturally by shutting off the oven. The resulting product was then collected by vacuum filtration and washed thoroughly with excess DMF to remove all the unreacted starting materials, followed by washing with DCM. The isolated product was transferred to a 20 mL scintillation vial with ~ 15 mL DCM for solvent exchange. After 24 h, the polycrystalline powder was isolated by vacuum filtration, washed with excess DCM, and then transferred to a 20 mL vial. The sample was then activated under dynamic vacuum at 150 °C for 24 h. The topology and phase change upon activation were confirmed for each mixed-linker framework by PXRD measurements (**Figure 4b–c, S4–S15**). The removal of adsorbed solvent upon activation was confirmed by ^1H NMR spectroscopy in $\text{DMSO-}d_6$ (**Figure S18–S35**). The ratio of linkers incorporated into the isolated frameworks were also determined from the ^1H NMR spectra of the digested frameworks (**Figure S18–S35**). The existence of the second linker in the mixed-linker system was confirmed by the characteristic stretches in the IR spectra (**Figure S36–S41**). The homogeneous distribution of the two linkers throughout the crystallites of the individual frameworks was confirmed by energy dispersive X-Ray (EDX) analyses (**Figure S42–S48**). Thermal stability was examined by

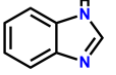
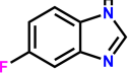
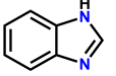
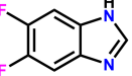
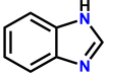
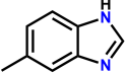
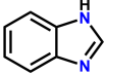
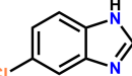
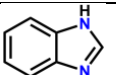
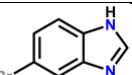
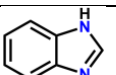
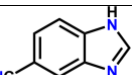
thermogravimetric analyses (TGA) (Table S1, **Figure S49**) showing little change between frameworks and differential scanning calorimetry (DSC) (**Figure S50**) measurements indicate that all twelve mixed-linker systems remain stable in their activated phase up to at least 390 °C.

2.3. Ambient Pressure Nitrogen, Carbon Dioxide, and Propane Adsorption Isotherms.

All ambient pressure nitrogen, carbon dioxide, and propane isotherms were carried out using a Micromeritics ASAP 2020 Plus instrument. Typically, ~150 mg of powdered activated samples was loaded into a pre-weighed analysis tube and sealed with a Micromeritics TransSeal. The tube was then attached to the degassing port for further evacuation for 24 h (Outgas rate < 5 μ bar/min at 150 °C). These fully degassed systems were then removed from degas port, weighed to determine the final sample mass, then transferred to the analysis port of the instrument, where the outgas rate was again confirmed to be less than 5 μ bar/min. Nitrogen and carbon dioxide isotherms were collected using a liquid nitrogen bath (77 K) and dry ice and acetone bath (195 K), respectively. Propane isotherms were collected at 25 °C using a temperature-controlled water circular bath from Julabo. The saturation pressure (P_0) was measured at every data point during nitrogen isotherm data collection and the average value was used for the relative pressure calculation. For carbon dioxide measurements, the saturation pressure was selected as ≈ 1.013 bar and relative pressures were calculated accordingly. During propane measurements, the temperature was manually inserted, and the instrument automatically adjusted the P_0 value based on its database from NIST. For all the propane isotherms at 25 °C, the P_0 value is ≈ 9.47 bar.

Table 1: Ratios of benzimidazole (bim) to substituted benzimidazole used in the synthesis, and those present in the resulting mixed-linker frameworks, as determined through post-digestion ^1H NMR spectroscopy. N/I = not included.

bim	substituted bim	Reaction time	Ratio in the synthesis	2.3:1	4:1	9:1
-----	-----------------	---------------	------------------------	-------	-----	-----

		24h	Ratio in the framework	3:1	5:1	10:1
		48h	Ratio in the framework	9:2	6:1	11:1
		72h	Ratio in the framework	7:2	6:1	14:1
		24h	Ratio in the framework	3:1	N/I	N/I
		48h	Ratio in the framework	7:2	N/I	N/I
		48h	Ratio in the framework	6:1	N/I	N/I

3. Results and Discussion

3.1. Synthesis and Structure Characterization

The baseline framework for this study, CdIF-13, is synthesized through prototypical solvothermal conditions, mixing benzimidazole and hydrated $\text{Cd}(\text{ClO}_4)_2$ (note: the weakly coordinating anion is apparently necessary given the relatively weak Cd–N bonds in the resulting framework) in *N,N*-dimethylformamide (DMF) and heating to 130 °C overnight, during which colorless crystals are formed. While this structure has been confirmed by SCXRD to show the same connectivity as ZIF-7, the DMF-saturated framework is distorted away from the high symmetry $R\bar{3}$ symmetry of the *sod* topology (**Figure 2a, b**),³⁴ which is thought to occur to maximize the heat of adsorption of the solvating DMF through ensemble interactions with the linkers (**Figure S2**). Upon solvent removal via activation under reduced pressure and elevated temperature, the framework switches to a denser phase with $P\bar{1}$ symmetry,³³ which has been characterized by SCXRD and PXRD to retain the same network connectivity, but exhibits significant skeletal distortion and linker rotation (**Figure 2c, d**). From the solved structure of the activated phase, we have inferred that inter-linker C–H $\cdots\pi$ and $\pi\cdots\pi$ interactions are the dominant

thermodynamic driving force for this switching to the denser, closed phase (**Figure 3**). Therefore, in the absence of adsorbate, the dense closed phase is more thermodynamically stable due to the presence of the exothermic C–H $\cdots\pi$ and $\pi\cdots\pi$ interactions (**Figure 3**). Upon increasing the pressure of some adsorbate there is a threshold at which the enthalpic favorability of adsorption can overcome these stabilizing inter-linker interactions causing the opening and saturation of the framework. We have also previously characterized through *in situ* powder neutron and X-ray diffraction that adsorption occurs primarily on the π -faces of the benzimidazolate benzene moiety, with the ring behaving as a Lewis base interacting electrostatically with regions of positive potential on the adsorbate molecules.³⁷ For example, with propane, we find that adsorption occurs through an ensemble of C–H $\cdots\pi$ interactions between benzene moieties and the alkane.³⁷

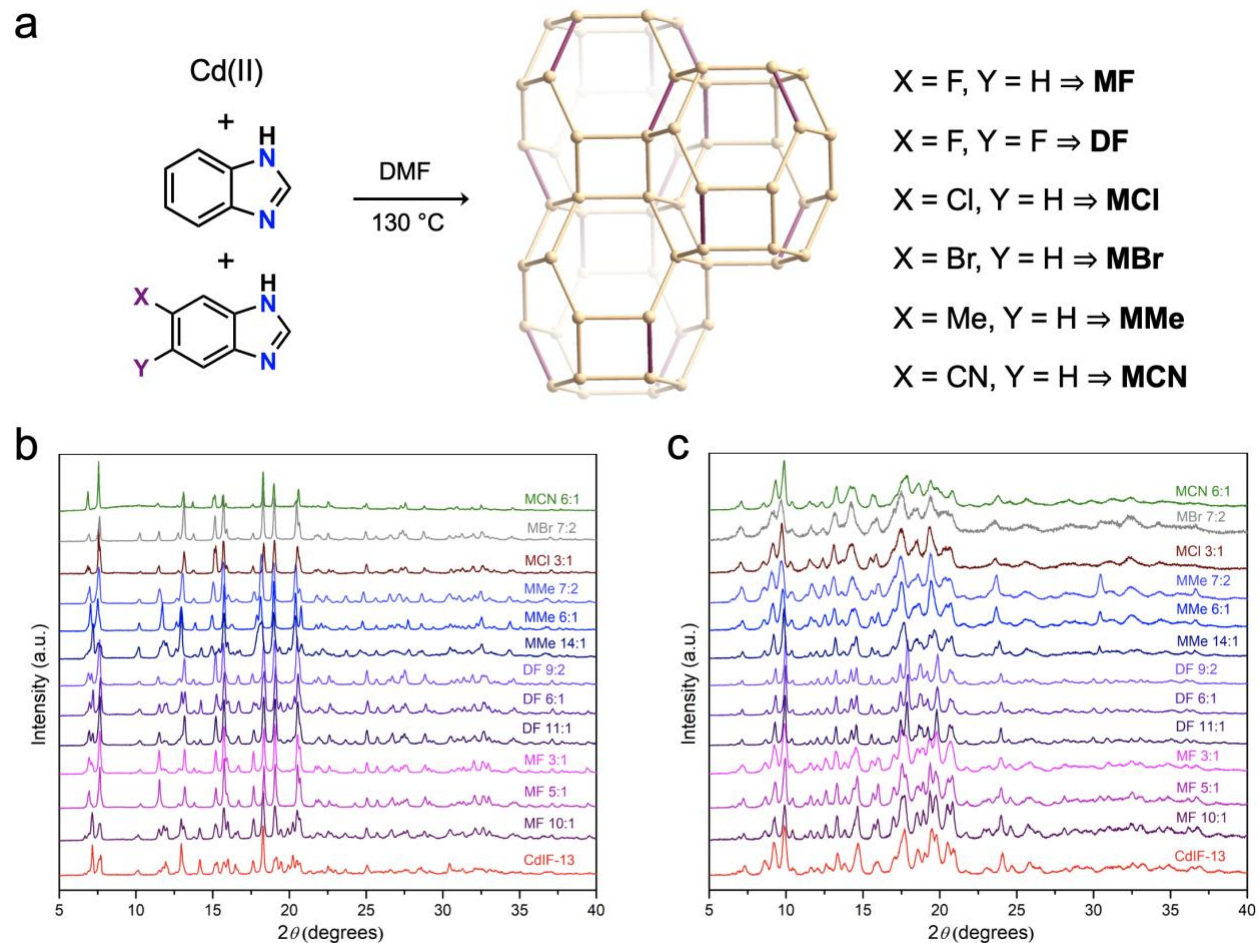


Figure 4. (Top) (a) General strategy for the synthesis of mixed-linker derivatives of CdIF-13. X and Y in the second benzimidazole linker represent the substitution used for the synthesis. Random distribution of the second linker, as characterized by EDX, is illustrated here by the inclusion of the purple lines in the topological presentation of the sodalite cages. (Bottom) PXRD patterns ($\lambda = 1.5406 \text{ \AA}$) of mixed-linker CdIF-13 (b) the DMF solvated phase and (c) activated phase. The PXRD studies reveal an isorecticular relationship with the parent CdIF-13 structure (depicted in red) in its solvated phase and goes through a similar structural flexibility upon activation. All patterns are also shown in the supporting information.

To test the influence of linker substitution and ratio, we selected six derivatives of benzimidazole which would appreciably affect the electrostatic potential surfaces of the linker, while attempting to minimize the steric bulk. Accordingly, 5-fluorobenzimidazole (**MF**), 5-chlorobenzimidazole (**MCl**), 5-bromobenzimidazole (**MBr**), 5-methylbenzimidazole (**MMe**), 5-cyanobenzimidazole (**MCN**), and 5,6-difluorobenzimidazole (**DF**) were chosen for this study. Using conditions adapted from those reported for CdIF-13, mixed-linker derivatives were synthesized spontaneously by the presence of both benzimidazole and the derivative linker in the synthesis mixture at a total amount equaling that of benzimidazole used for CdIF-13. The mixtures were again heated in DMF, being left for varying durations until appreciable solid product was observed. Upon isolation, the solvated samples were first characterized by PXRD (**Figure 4b**) to confirm that the *sod* topology was indeed produced.

We wish to highlight observed differences between the observed patterns of the solvated frameworks, most apparent in the reflections centered around $7.5 \text{ } 2\theta$ ($\lambda = 1.5406 \text{ \AA}$). These differences are the result of the aforementioned distortion of the solvated framework away from the ideal $R\bar{3}$ symmetry of the *sod* topology. Wherein greater observed splitting of reflections results from greater distortion and lower symmetry of the DMF-solvated phase. The observed pattern of

the DMF-solvated phase is sensitive to the precise procedure of used for these measurements, with varying instrument temperatures and handling times leading to varying degrees of solvation and thus structural symmetry. However, given previous work with CdIF-13, including SCXRD-based confirmation of the DMF-solvated structure and the resulting simulated PXRD pattern (**Figure 4b, S3**),³⁴ we can confidently state that all the observed patterns are indeed representative of the desired framework connectivity in the low-density, open phase with high accessible porosity.

The as-synthesized DMF-solvated frameworks were then activated by solvent exchange with CH₂Cl₂ (DCM) followed by heating under dynamic vacuum. Full solvent removal was confirmed by digestion with deuterated hydrochloric acid (DCI) in D₂O and subsequent solution-phase ¹H NMR spectroscopy in DMSO-*d*₆ (**Figure S17–35**). The ratio of linkers incorporated into the respective synthesized mixed-linker frameworks could be simultaneously quantified through integration of respective protons present on the benzene and imidazole rings (**Figure S17–35**). While the ratio of linkers incorporated into the lattice are indeed influenced by the starting ratios in the synthesis mixture, they do deviate from these ratios, as detailed in **Table 1**. We hypothesize that this is the result of differences in coordination strength as influenced by the substituent, affecting both initial rate of incorporation as well as the dynamic bonding known to be key in crystal growth. Nonetheless we can construct a catalog of twelve mixed-linker derivatives of CdIF-13, composed of three three-member series of varying ratios and three additional frameworks. With five of the six substituted linkers, a mixed-linker derivative with a close to 3:1 ratio (benzimidazole:substituted benzimidazole) was obtained, permitting direct comparison of the effect of substitution at a specific ratio. With 5-cyanobenzimidazole, 6:1 ratio was the lowest obtainable ratio. However, due to the common use of cyano substitution in porous frameworks, its inclusion was deemed relevant.

Part of the selection process for the twelve chosen frameworks, from the 50 or so synthesized, is that they exhibit a very similar phase change to CdIF-13 upon activation (**Figure 4c**).^{33, 34} At higher percentages of the substituted linker, there tends to be a loss in the full flexibility of the framework, ostensibly due to some combination of steric bulk in this dense topology and electronic effects on the inter-linker and adsorbate–linker interactions. These effects were discussed in detail in our previous report focused solely on mixed-linker series with 2–methyl–5,6–difluorobenzimidazole.³⁶ For the 12 structures discussed herein, PXRD patterns of the activated frameworks confirm that each undergoes a phase change to a lower symmetry phase analogous to that of CdIF-13, which is most prominently indicated by a quartet of reflections between 8–11 2θ ($\lambda = 1.5406 \text{ \AA}$) and has been previously characterized by SCXRD (**Figure 4c**).^{33, 34}

3.2 Isothermal Gas Adsorption Measurements

The observation of reversible phase changes upon activation (**Figure 4c**) and resolution (**Figure S16**) by PXRD is the mark of structural dynamics, but not necessarily of periodic flexibility or of step-shaped adsorption. To confirm the retained first-order cooperative phase change in each mixed-linker derivative and explore the influence of substitution and linker ratio on the resulting step-shaped profile, equilibrium isothermal gas adsorption measurements were performed with a series of probe gases of varying size, shape, and electrostatic surface potentials. For CdIF-13 and each of the twelve mixed-linker derivatives, measurements were collected for N₂ at 77 K (**Figure 5**), CO₂ at 195 K (**Figure 6**), and propane at 298 K (**Figure 7**), with the first two being prototypical probes at their respective boiling point and the third being a probe we have studied extensively with CdIF-13 in our work exploring olefin–paraffin separations³⁷. We note that adsorption capacities are shown in mol/mol to control for framework mass changes and allow for direct observation of effects on capacity.

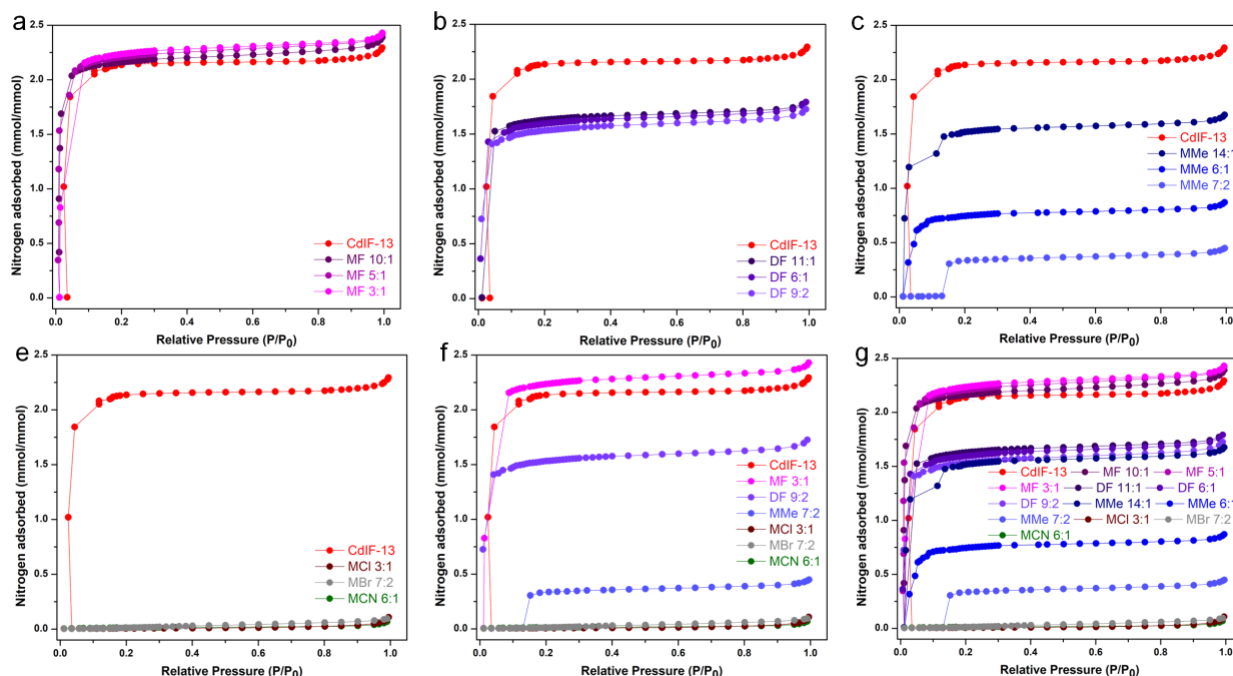


Figure 5. Isothermal adsorption measurements for N_2 at 77 K for parent CdIF-13 and the 12 mixed-linker derivatives. (a) CdIF-13 and three ratios with **MF**. (b) CdIF-13 and three ratios with **DF**. (c) CdIF-13 and three ratios with **MMe**. (d) CdIF-13 and one framework with each **MCN**, **MCl**, and **MBr**. (e) CdIF-13 and the framework with the lowest accessible ratio of each substituted linker. (f) Overlay of data for all thirteen frameworks. The connecting lines between data points are not mathematical fits but to guide the eye only. Full adsorption-desorption profiles for individual frameworks are presented in **Figure S51–63**. Average $P_0 = 828.785$ mbar.

3.2.1. N_2 at 77 K: CdIF-13 exhibits minimal adsorption until an approximate threshold of relative pressure (P/P_0) 0.03, at which a saturation capacity of 2.1 mol/mol occurs by $P/P_0 = 0.15$ (**Figure 5, S63**). In the case of the three-member series with both **MF** (*i.e.*, 10:1, 5:1, and 3:1) and **DF** (*i.e.*, 11:1, 6:1, and 9:2), no pre-step adsorption regime is observed, with only sharp saturation at very low pressures being observed (**Figure 5a, b**). Based on results discussed below with CO_2 and propane, we hypothesize that step-shaped adsorption is still occurring, however the threshold pressure is too low to be readily observed without immense data density in the microbar regime or

measurements at elevated temperatures. The three-member series with **MMe** (*i.e.*, 14:1, 6:1, and 7:2) exhibits quite a different trend (**Figure 5c**). At 14:1, saturation again occurs without an observable pre-step, however we also observe the onset of what we hypothesize to be a second step. This observation is not entirely unexpected, as two-step adsorption is observed for CdIF-13 with CO₂ at 195 K (see below) and is indicative of an intermediate structure stabilized under specific pressure–temperature conditions. At 6:1, no observable second step occurs. At 7:2, not only is there no observable second step, but the threshold of the first step has shifted to a higher pressure than CdIF-13. In addition to affecting the adsorption behavior, we expect the relatively large size of the –CH₃ substituent to be a key contributor to the observed reductions in mol/mol capacity. In contrast to these three series, each of the other derivatives, ~ 3:1 with **MCl** and **MBr** and ~ 6:1 with **MCN**, exhibit negligible adsorption up to 1 bar, suggesting that the adsorption threshold is beyond the measurable pressure window at 77 K (**Figure 5e**). Through these adsorption measurements with N₂ at 77 K, we can clearly see the large impact mixed-linker derivation can have on adsorption behavior, even when flexibility is apparently constant by PXRD, inducing both dramatic reductions in the threshold pressure and the complete absence of adsorption.

3.2.2. CO₂ at 195 K: CdIF-13 exhibits minimal adsorption until an approximate threshold of $P/P_0 = 0.02$, at which a saturation capacity of ~ 1.5 mol/mol is reached by $P/P_0 = 0.10$ (**Figure 6, S76**). In contrast to N₂ at 77 K, this is followed by a second step near $P/P_0 = 0.25$, with a saturation capacity of 2.1 mol/mol reached by $P/P_0 = 0.34$. Given the low-pressure threshold of the first step, relatively small changes in apparent step and saturation pressures are observed with the mixed-linker derivatives (**Figure 6, S64–S75**), and thus strong conclusions on their relative behavior are

difficult to make in most cases. However, we observe significant changes to the position, profile, and/or presence of the second step. Overall, both the **MF** and **DF** series exhibit a similar trend,

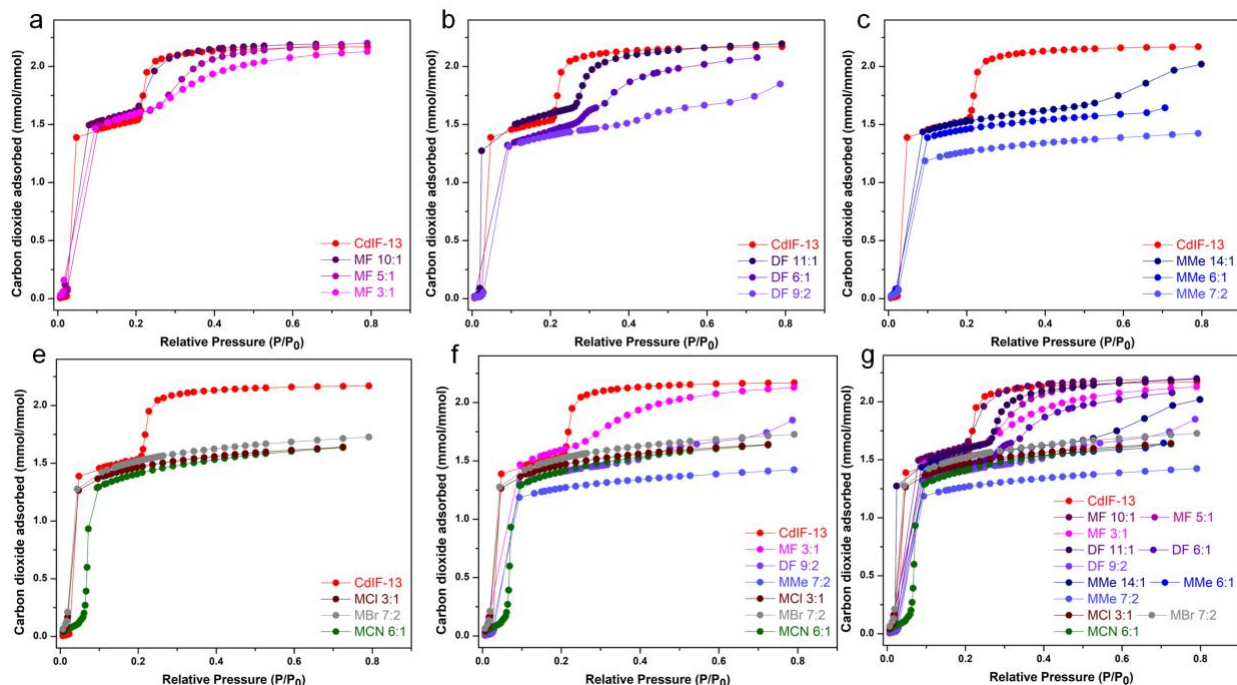


Figure 6. Isothermal adsorption measurements for CO₂ at 195 K for parent CdIF-13 and the 12 mixed-linker derivatives. (a) CdIF-13 and three ratios with **MF**. (b) CdIF-13 and three ratios with **DF**. (c) CdIF-13 and three ratios with **MMe**. (d) CdIF-13 and one framework with each **MCN**, **MCl**, and **MBr**. (e) CdIF-13 and the framework with the lowest accessible ratio of each substituted linker. (f) Overlay of data for all thirteen frameworks. The connecting lines between data points are not mathematical fits but to guide the eye only. Full adsorption desorption profiles for individual frameworks are presented in **Figure S64–S76**. $P_0 = 1.013$ bar.

with the highest ratio derivative exhibiting a lower pressure first step than CdIF-13, and a second step of similar shape to CdIF-13 near or just below the same threshold pressure (**Figure 6a, b**). However, at the two lower ratios in both series, the first step appears to shift back to higher pressures. More substantially, the second step becomes much more gradual, to a point that one can argue that the lowest ratio frameworks show no step at all. For the **MMe** series, we again observe

relatively subtle effects on the first step (**Figure 6c**) and large effects on the second, with the highest ratio framework only exhibiting a broad step at much high pressures, and the lower two ratio frameworks exhibiting no second step in the measurable pressure window. Rather, maintaining a very flat capacity, suggesting there is no gradual phase change after the first step like that observed with the **MF** and **DF** series. The 3:1 **MCI** and **MBr** frameworks exhibit very similar behavior, with a slight reduction in the threshold of the first step, with saturation by about $P/P_0 = 0.1$ (**Figure 6d**). This is followed by a flat capacity throughout the measurable window, like the lower two ratio frameworks with **MMe**. In slight contrast, the 6:1 **MCN** derivative shows a similar threshold pressure to CdIF-13 for the first step. However, the post-step region is again quite flat across the measurable window, indicating no post-step increase in accessible porosity (**Figure 6d**). The five ~ 3:1 derivatives show a narrow observable difference in the onset of the first step, with only the 3:1 framework of **MF** showing appreciable post-step adsorption, albeit in gradual manner. In total, derivation of CdIF-13 results in subtle effects to the first adsorption step with CO₂ at 195 K, but significant alterations to the second step, including broadening and complete absence.

Propane at 298 K: CdIF-13 exhibits minimal adsorption until an approximate threshold of $P/P_0 = 0.025$, at which a saturation capacity of 0.81 mol/mol is reached over a particularly narrow pressure regime, followed by an effectively flat post-step regime (**Figure 7, S89**). In contrast to both the N₂ and CO₂ measurements, we observe a very similar adsorption profile for all twelve derivatives, with only the adsorption threshold pressure and capacity changing (**Figure 7, S77–88**). Owing to the relatively high adsorption threshold pressure for CdIF-13, changes to the adsorption threshold of propane at 298 K in the mixed-linker derivatives is quite apparent. For both the **MF** and **DF** series, a significant jump to lower pressure for the adsorption threshold is

observed at even the highest ratios (i.e., 10:1 and 11:1, respectively) (**Figure 7a, b**). This is followed by a more subtle lowering of the adsorption threshold

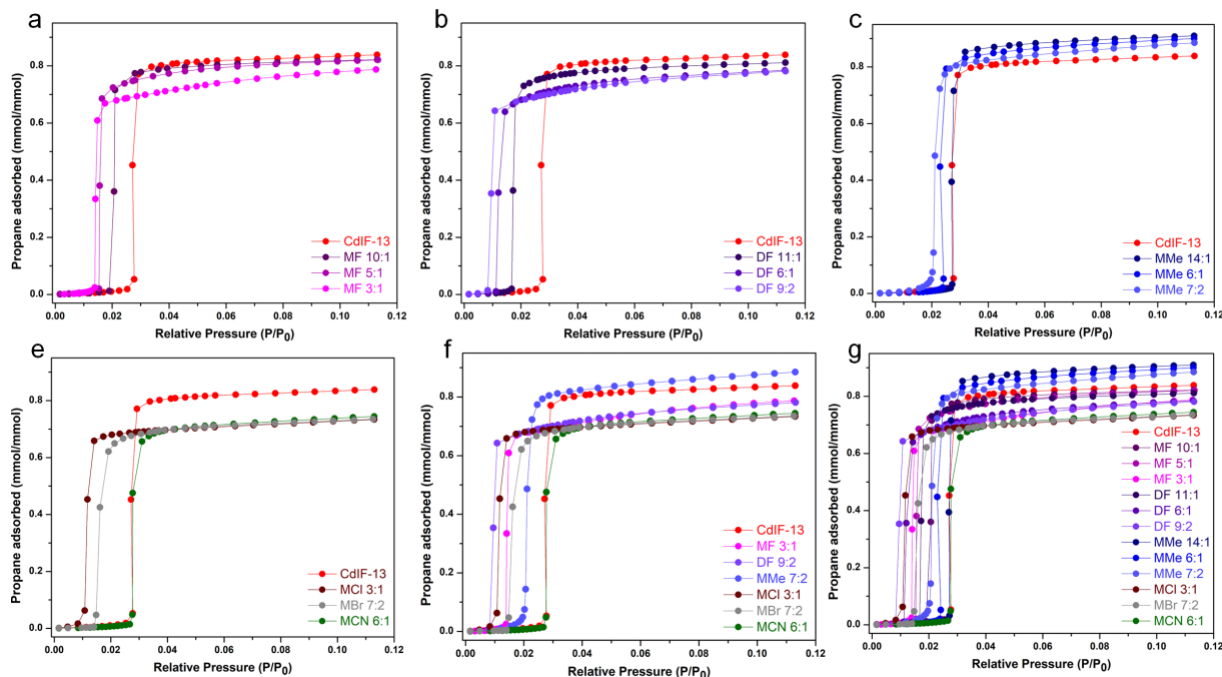


Figure 7. Isothermal adsorption measurements for propane at 298 K for parent CdIF-13 and the 12 mixed-linker derivatives. (a) CdIF-13 and three ratios with **MF**. (b) CdIF-13 and three ratios with **DF**. (c) CdIF-13 and three ratios with **MMe**. (d) CdIF-13 and one framework with each **MCN**, **MCI**, and **MBr**. (e) CdIF-13 and the framework with the lowest accessible ratio of each substituted linker. (f) Overlay of data for all thirteen frameworks. The connecting lines between data points are not mathematical fits but to guide the eye only. Full adsorption-desorption profiles for individual frameworks are presented in **Figure S77–89**. $P_0 = 9.47$ bar.

pressure for the other two members of each series, with the 5:1 and 3:1 members of the **MF** series exhibiting quite similar threshold pressures (**Figure 7a**), as do the 6:1 and 9:2 members of the **DF** series (**Figure 7b**). In the **MMe** series, we again observe reduction in the adsorption threshold pressure with increasing presence of the methylated linker (**Figure 7c**). However, the effects are lesser than with fluorination, with the 7:2 member of the **MMe** series having a higher threshold

than even the 11:1 member of the **DF** series (**Figure 7g**). Like the fluorinated frameworks, the 3:1 **MCl** and **MBr** derivatives exhibit a significantly reduced threshold, with **MCl** being lower than both 3:1 **MF** and **MBr** at about $P/P_0 = 0.011$ (**Figure 7e**). In contrast, the 6:1 **MCN** derivative exhibits effectively no change to the adsorption threshold, only lowering the total capacity. For the series of five ~ 3:1 mixed-linker derivatives, the four halogenated systems show dramatic reductions in the adsorption threshold pressure, with the **MMe** derivative sitting closer to that of CdIF-13 (**Figure 7e**). Whereas the N₂ at 77 K and CO₂ at 195 K data sets exhibit seemingly complex combinations of changes to pressures, capacities, shapes, and number of steps, the data set for propane adsorption at 298 K is relatively simple, providing a more semi-quantitative story of the influence of linker substitution and ratio.

3.3 Analyzing the Influence of Substitution and Linker Ratios on Cooperative Flexibility and Adsorption Behavior

From the preceding isothermal gas adsorption measurements with N₂ at 77 K, CO₂ at 195 K, and propane at 298 K, the significant and diverse influence of linker substitution on adsorption behavior is apparent, even when flexibility is consistent as characterized by PXRD. By making use of the mixed-linker approach, we can not only produce a larger catalog of derivatives that are functionally distinct, but also a catalog that can be leveraged for more systematic fundamental investigations of flexibility. Although outside the scope of this specific report, *in situ* variable pressure PXRD measurements would ideally be performed for each combination of adsorbate and adsorbent at a synchrotron to provide high quality data from which atomic-level structure of the framework and adsorbate could be refined. Additionally, high level computational analysis, well beyond our own capabilities, of the 13 total frameworks and 39 adsorption data sets could be powerful for advancing our understanding. Particularly with an eye to understanding how

substitution affects the relative energy of the closed and saturated open states and the activation barrier between them that is thought to regulate the adsorption threshold pressure. In the absence of such measurements and calculations, we can infer certain relationships based on our knowledge of the closed and open structures of CdIF-13, influence of substituents on the electrostatic potential surface of benzimidazolate, and, in the case of propane, how the gas interacts with the pore surface.

The following interpretations are based largely on insights gained from our previous studies on CdIF-13. Namely, we have characterized by SCXRD both the fully activated closed phase (**Figure 2c, d**)³³ and DMF-solvated open phase of CdIF-13 (**Figure 2a, b**),³⁴ including the solvent position (**Figure S2**), providing insights into interactions that stabilize both states. We have also characterized the propane-saturated structure of CdIF-13 by Rietveld refinement of data collected from *in situ* variable pressure synchrotron PXRD, including the adsorbed propane molecules.³⁷ This shows that propane adsorption occurs through an ensemble of contacts with the π -rich faces of the benzimidazolate linkers with C–H bonds of the alkane. From these structures, we can infer the interactions that serve to stabilize the closed phase, and, in the case of propane, those that stabilize the open phase. Namely, side-on and face-on inter-linker C–H $\cdots\pi$ and $\pi\cdots\pi$ interactions (**Figure 3**) and adsorbate–linker C–H $\cdots\pi$ interactions in which the π -rich linker acts as a Lewis base (**Figure 8a, S97**), respectively. Below we first analyze the effects of substitution on the linker electronics, then discuss how the respective gases are expected to be adsorbed at the atomic level in this group of frameworks. This is then followed by a group-by-group analysis of apparent trends with proposed explanations for these observations.

3.3.1. Effect of Substitution on Linker Electrostatic Potential Surfaces

To help analyze the influence of the linker substitutions on these variables, we first turn to DFT-based calculations of the electrostatic potential (ESP) surface map of benzimidazolate and

how substitution affects the distribution and magnitude of regions of positive (*i.e.*, Lewis acidic) and negative (*i.e.*, Lewis basic) surface potential. From the electronic potential surface maps, we found that a significant negative potential is distributed over the two nitrogen atoms (**Figure 8, S90–96, Table S3–S9**), exactly what is necessary to coordinate to two Cd(II) centers and make a framework. Apart from the nitrogen atoms, the π -faces of the arene ring exhibits negative potential, with the outer edges of the C–H bonds being the most positive region in potential, aligning with C–H σ^* orbitals (**Figure 8, S90–96**). While methyl substituents are considered donating by Hammett substitution constants, the calculated change in the surface potential of the π -faces of the arene rings is relatively minor (**Figure 8d, S93, Table S6**). Perhaps more relevant, are the new regions of slightly positive potential present on hydrogen atoms of the methyl group, again correlating to C–H σ^* (**Figure 8d, S93, Table S6**). Fluorination results in a significant reduction in the negative potential of the π -faces and increase in the positive potential of the hydrogen atoms (**Figure 8b, S91, Table S4**). Both trends are exasperated upon introduction of the second fluorine atom (**Figure 8c, S92, Table S5**), with the addition of a strong negative potential in between two F-atoms. Given the significant

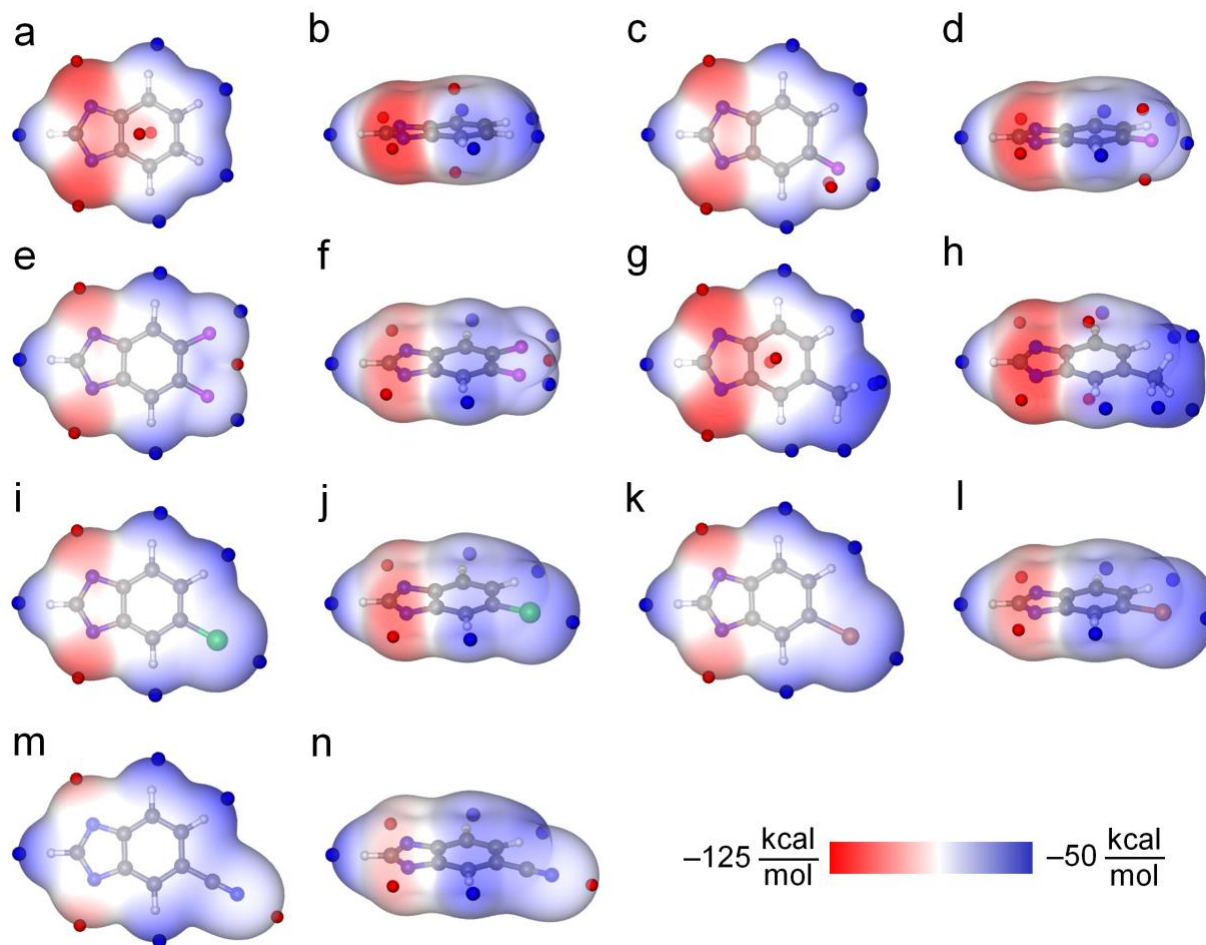


Figure 8. DFT-generated electrostatic potential (ESP) maps of geometry-optimized (a,b) benzimidazole, (c,d) 5-fluorobenzimidazole (**MF**), (e,f) 5,6-difluorobenzimidazole (**DF**), (g,h) 5-methylbenzimidazole (**MMe**), (i,j) 5-chlorobenzimidazole (**MCl**), (k,l) 5-bromobenzimidazole (**MBr**), and (m,n) 5-cyanobenzimidazole (**MCN**), calculated at the $0.001 e^- \text{ bohr}^{-3}$ isosurface. Both the top-view and side view are shown for clarity, with (a, c, e, g, i, k, and m) a top view and (b, d, f, h, j, l, and n) a side view of the individual linkers. Regions of positive potential are depicted in blue and regions of negative potential are depicted in red. Dark blue and red spheres indicate the $V_{s,\text{max}}$ and $V_{s,\text{min}}$, respectively. Grey, dark blue, magenta, green, orange, and white spheres represent C, N, F, Cl, Br and H, respectively.

drop in electronegativity from F to Cl and Br (Pauling Scale, F = 3.98, Cl = 3.16, Br = 2.96, C = 2.55, H = 2.20), chlorination (**Figure 8e**, **S94**, **Table S7**) and bromination (**Figure 8f**, **S95**, **Table**

S8) of benzimidazolate is less impactful on the surface potentials of the π -faces and H atoms than fluorination. However, these atoms still exhibit appreciable negative potentials, and are more polarizable than F, meaning they are more prone to forming exothermic dispersion interactions in addition to the electrostatic contacts predicted from ESP maps. Finally, the very strong electron withdrawing nature of the cyano functional group, as intimated by its very positive Hammett substitution constant, results in a surface potential map that is effectively between that of mono-fluoro and di-fluorobenzimidazolate. In addition, the N atom of the cyano moiety has particularly negative potential, given the two polarized π bonds of the cyano triple bond and the *sp* lone pair on the N atom itself (**Figure 8g, S96, Table S9**).

3.3.2. Adsorbates

3.3.2.1. CO₂

It was previously reported for ZIF-7, the predecessor Zn(II)-based congener to CdIF-13, that CO₂ adsorption at 195 K occurred in a two step-fashion, wherein the two distinct steps result from sequential opening at the two different types of 6-membered pore windows present in the framework.^{38, 39} These two pores are analogous to the blue and magenta pore windows highlighted for CdIF-13 in **Figure 2**. Additionally, *in situ* neutron diffraction experiments with ZIF-7 suggest that both the electrostatically negative O atoms and positive C atom of CO₂ play a role in adsorption, interacting with the electrostatically positive H atoms and negative π -face of the linker, respectively. Accordingly, our analysis of CO₂ adsorption in the mixed-linker derivatives of CdIF-13 will be strongly influenced by these prior studies with ZIF-7.

3.3.2.2. Propane

In our recent study on the ability of CdIF-13 to selectively adsorb ethane over ethylene and propane over propylene we performed *in situ* synchrotron PXRD measurements.³⁷ The high quality of the diffraction data permitted refinement of the atomic positions of propane in the saturated framework in both aforementioned six-membered pore windows (**Figure 2, S97**). In both cases, we observe individual propane molecules interacting with the π -rich faces of the linkers through an ensemble of C–H $\cdots\pi$ interactions (**Figure S97**). Accordingly, changes to the magnitude and distribution of surface potential on the linkers should appreciably affect the strength and manner in which adsorption occurs.

3.3.2.3. N₂

Little prior work on how N₂ is adsorbed in either CdIF-13 or ZIF-7 has been done. Thus, our interpretations of observed effects on N₂ adsorption behavior will be based in our cumulative understanding of the adsorption of CO₂ and propane, assuming weak interactions with the frontier electrons and π^* orbitals (*i.e.*, HOMO and LUMO) of N₂.

3.3.3 Group-By-Group Analysis of Linker and Ratio Effects

Please note that we wholly acknowledge that the following analyses/hypothesis are not unambiguously supported by experimental results but are put forth to help guide future analysis that may be supported by *in situ* diffraction or advanced computational studies.

3.3.3.1 MF and DF Series

We have chosen to combine our analysis of the two three-membered groups of mixed-linker derivatives with **MF** and **DF** owing to the very similar observed trends. For the adsorption of N₂ at 77 K, a significant shift to lower threshold pressures occurs for all six derivatives. However, due to the how low this apparent threshold is for each framework, it is difficult to resolve the apparent differences between them (**Figure 5a, b**). For propane at 298 K, all six frameworks again exhibit

a significantly reduced adsorption threshold, but, in this case we can distinguish that a progressive shift to lower thresholds occurs with increasing presence of the fluorinated linkers (**Figure 7a, b**). In each case we suspect that the primary culprit of the observed behavior is the effective destabilization of the closed phase. Given the hypothesis that the inter-linker C–H $\cdots\pi$ and $\pi\cdots\pi$ interactions are the primary stabilizing entity for the closed phase, the net strength of these interactions is directly correlated to the pressure threshold at which they are broken, an endothermic event compensated for by exothermic adsorption. Modulating this exothermic heat of adsorption ($-\Delta H_{\text{ads}}$) also affects the threshold pressure, as is apparent by the need to cool to 77 K to observe uptake of weakly adsorbing N₂ below 1 bar, whereas more strongly adsorbed propane causes framework opening below 1 bar at 298 K. Thus, we hypothesize that this threshold reduction is strongly influenced by how the presence of the fluorine atoms causes repulsive interactions in the closed phase. This arises as fluorinated arenes have an inverted surface potential distribution relative to wholly protonated arenes (**Figure 8a–f, S90–S92 Table S3–S5**). Thus, the two motifs will electrostatically repel each other when forced to be face-to-face or side-to-face, as they are in the closed structure of CdIF-13 (**Figure 2c, d**). These repulsive interactions destabilize the closed phase, leading to a lower energetic barrier to opening and, therefore, lower adsorption thresholds.

In the case of CO₂ at 195 K, there appears to be an inverted trend with increasing fluorination for both the first and second step, as well as significant effect of fluorination on the shape and altogether presence of the second step (**Figure 6a, b**). An appreciable drop in the pressure threshold of the first step is again observed with the highest ratio of members for each series. However, with increased presence of the fluorinated linkers, this shifts back towards that of CdIF-13. Given what was observed for N₂ and propane with this series (**Figure 5a, b, 7a, b**), namely

shifting to lower pressure thresholds, we would suspect that this divergent observation is caused by a significant change to the adsorption behavior, namely a weakening of $-\Delta H_{\text{ads}}$. All previously characterized adsorption in ZIF-7 and CdIF-13 has been shown to occur on the faces of the linkers within the effective “pocket” of the pore window,^{25,33,37} and we know from structural analysis that the fluorine atoms will be on the periphery of this pocket.³⁶ Thus, we suspect they do not directly participate in adsorption, rather, they only serve to make the surface of the linkers more positive, thus making the surface interactions with CO₂ less favorable.

As for the second step, the increasing presence of the fluorine atoms in the lattice appears to have a more significant effect. For the **MF** series we see a lowered threshold at the highest ratio (10:1), but this step returns to higher pressures near that of CdIF-13, with dramatic broadening of the step (**Figure 6a**). This broadening is likely the result of a lowering of the activation barrier between the two end states and/or the introduction of additional meta-stable intermediate states, again with lowered activation barriers between them. That is to say that pore opening happens in a more gradual fashion as pressure is increased, rather than jumping between two states in a discontinuous fashion. In the **DF** series, this trend is even more apparent, wherein the highest ratio framework (11:1) still has a sharp step near that of CdIF-13, but at 6:1 and 9:2 this is dramatically broadened to the point that there is no apparent step for the 9:2 framework. Rather, there is just a gradual increase in capacity that is still occurring at the highest pressure data point (**Figure 6b**). Again, this suggests that increasing fluorination is affecting the energy barriers between structural states, obviating the first order phase change we see for CdIF-13.

3.3.3.2. MMe Series

When considering the influence of the methyl substituent, we suspect there are three primary factors at play. First that the methyl group’s three C–H bonds can introduce additional C–H $\cdots\pi$

interactions to the framework in the closed phase, causing stabilization, as was observed for the methylated derivative of Co(bdp).³⁰ Second, that the three dimensional nature of the methyl group (*i.e.*, tetrahedral) could sterically prevent full closing of the pore window, destabilizing the closed phase. Third, that the electron-donating nature of a methyl substituent increases the negative electrostatic potential of the arene π -faces, leading to stronger $-\Delta H_{\text{ads}}$, lowering adsorption thresholds.

With propane at 298 K, there is a relatively small shift to lower adsorption thresholds, with the lowest ratio (7:2) having about the same adsorption pressure threshold as the highest (10:1) in the MF series (**Figure 7a, c**). We suspect this is the result of the competition between opposing actors. Specifically, that the richer π -faces enhance the strength of C–H $\cdots\pi$ interactions with propane (**Figure S97**), lowering the threshold, but the magnitude of this change is tempered by increased inter-linker C–H $\cdots\pi$ interactions with increasing presence of methylation. Ultimately resulting in relatively offsetting effects and small changes to the step position.

When considering the first adsorption step in the CO₂ at 195 K measurements, we again see a relatively small effect at the highest (14:1) and lowest (7:2) ratios, with the middle ratio (6:1) appearing as an outlier, with an appreciably reduced threshold. We hypothesize that this is the result of the competing phenomena discussed above. Specifically, that at 14:1 and 6:1, the increased presence of π -rich linkers increases $-\Delta H_{\text{ads}}$, progressively shifting the threshold pressure lower. But, at 7:2, where there is statistically at least one methylated linker per pore window, the enhanced interactions between linkers stabilizes the closed phase, pushing the threshold pressure back towards that of CdIF-13. As for the second step, which is suspected to be the opening of the six-membered ring with all linkers pointing in (magenta, **Figure 2b, d**) based on previous work with ZIF-7,³³ the effects are more significant; Being pushed out too much higher pressures and

broadened at the highest ratio, and all together absent with no gradual increase for the lower two. Given the likely abundance of both face-to-face and side-to-face C–H $\cdots\pi$ interactions in this pore window relative to the yellow and blue pores (**Figure 2b, d**), we suspect that methylation further stabilizes the closed phase of this pore, precluding observable opening and adsorption in the measurable pressure window.

The adsorption behavior of the methylated derivatives for N₂ at 77 K is particularly complex (**Figure 5c**). However, we hypothesize that the observed adsorption profiles can be explained similarly to CO₂ and are not the result of large steric effects on accessible porosity. Namely, that there is an initial enhancement of adsorption strength leading to a lower pressure first step, followed by enhanced stability of the three six-membered pores in which adsorption occurs (*i.e.*, magenta, blue, yellow, **Figure 2**) with increasing methylation. Moreover, with the relatively weak $-\Delta H_{\text{ads}}$ of N₂ and differences in the type and quantity of inter-linker contact in the three pores (**Figure 3**), this results in the single step observed for CdIF-13 being separated into distinct steps. We note that diverse multi-step behavior with N₂ has been observed previously in cooperatively flexible frameworks, as reported for Co(bdp) and its functionalized derivatives. With each Co(bdp) derivative showing a distinct multi-step adsorption profile resulting from linker-dependent differences in meta-stable intermediate phases, wherein the exothermic adsorption balances endothermic phases changes.^{30, 40} Accordingly, we hypothesize that in the highest ratio (14:1) framework with **MMe**, the yellow and blue-labeled pores with fewer apparent inter-linker interactions in the closed phase open at a lower pressure due to stronger adsorption, followed by a second step arising from the relatively stabilized closed magenta-labeled pore that exhibits more inter-linker contacts (**Figure 3**). In the middle ratio (6:1) **MMe** framework, this first step appears to broaden to higher pressures, with no apparent second step occurring, suggesting that the greater

methylation leads an inability for N₂ adsorption to overcome the enhanced stability of the closed form of the magenta-labeled pore. Finally, at the lowest ratio (7:2), again with the statistical presence of at least one methylated linker per pore window, we observe a dramatic shift in the first step beyond that of CdIF-13, followed by a much smaller, but still sharp, step. We hypothesize this is due to both the magenta- and blue-labeled pores, with their clear inter-linker C–H··· π and π ··· π interactions remaining closed in the measurable window. While the yellow-labeled pore, with only face-to-face linker interactions possible, can be opened, if only partially.

Overall, we hypothesize that the weak $-\Delta H_{\text{ads}}$ of N₂ makes its adsorption profile, relative to that of more strongly adsorbing CO₂ and propane, particularly susceptible to the effects of methylation. These data sets also appear to suggest that the way adsorption occurs for these three gases is considerably different. With variances in size and surface potential causing different interactions at the distinct pores of the framework, which themselves vary in shape, size, and presence of stabilizing inter-linker interactions.

3.3.3.3. Lowest Ratio Series

We finally examine the relative behavior of the five approximately 3:1 mixed-linker derivatives (i.e., **MF**, **DF**, **MMe**, **MCl**, and **MBr**) and one **MCN** derivative containing the lowest achievable ratio, 6:1 (**Figure 5f**, **6f**, **7f**).

For propane at 298 K, the **MCl** and **MBr** derivatives exhibit very reduced adsorption threshold pressures (**Figure 7e**, **f**). In fact, the **MBr** derivative has an adsorption threshold near the 3:1 **MF** framework, with the **MCl** analog exhibiting an even lower threshold, being only surpassed by the 9:2 **DF** derivative (**Figure 7e**, **f**). The threshold pressures for **MBr** and **MCl** being similar to and even lower than the **MF** analog, respectively, is initially surprising owing to the relative electronegativities of the respective halogens and calculated effects of the π -face of the linkers

(**Figure 8, S91, S94, S95**). However, at this low ratio, the **MF** system is likely to form strong interactions between fluorinated linkers (i.e., $F\cdots\pi$ -hole), leading to the threshold pressure increasing as the co-localization of fluorinated rings becomes more likely. We hypothesize that strong interactions between substituted linkers is also present in the **MCN** derivative (i.e., $C-N\cdots\pi$ -hole), leading to an adsorption threshold near that of CdIF-13 despite the large positive potential on the cyano-benzimidazolate linker π -face (**Figure S96, Table S9**) repelling the C–H moieties of unfunctionalized benzimidazolate.

A very similar trend is observed for the first adsorption step for CO_2 at 195 K. However, for all three of the additional frameworks, **MCl**, **MBr**, and **MCN**, the second step observed for CdIF-13, assumed to be the opening of the magenta pore window owing to the larger number of apparent inter-linker interactions (**Figure 3**), is completely absent, akin to the 7:2 **MMe** analog. At this low ratio there is a high probability of interactions between two of the substituted linkers, and with the lower electronegativity and greater polarizability, therefore Lewis basicity, of the chlorine and bromine substituents relative to fluorine, they can form strong interactions with electronic contributions beyond electrostatics. In the case of the cyano-substituted ring, there is such a large increase in the positive electrostatic surface potential of the linker π -faces, that very strong side-to-face electrostatic interactions with the very negative N atom of the cyano group could occur, precluding opening of this pore.

Finally, for N_2 at 77 K, the complete absence of adsorption is observed for the **MCl**, **MBr**, and **MCN** derivatives (**Figure 5e, f**). Like the second step for CO_2 at 195 K, the behavior of these derivatives is more akin to the 7:2 **MMe** derivative than either of the fluorinated analogs (**Figure 5f**). While the 9:2 **DF** and 3:1 **MF** frameworks exhibit a reduction in the adsorption pressure threshold, 7:2 **MMe** has only a partial step, which occurs beyond that of CdIF-13. Therefore, we

analogously propose that this lack of adsorption (**Figure 5f**) and remaining in the fully closed state is caused by the combined weak $-\Delta H_{\text{ads}}$ of N_2 and the stronger interactions between two of the substituted linkers that is likely to occur at these low ratios.

4. Conclusion

Our limited understanding of cooperative flexibility in metal–organic frameworks currently precludes the ability to deliberately derivatize known frameworks for specific applications, let alone targeted *de novo* design. We believe that a primary issue holding back the advancement of this understanding is a dearth of systematically varied data sets with minimized variables that cannot be controlled for. This is the result of the current serendipitous discovery of flexible frameworks, the immense diversity in the structure, composition, and mode of flexibility of these frameworks, and the finite amount of diversification that can be achieved through complete metal substitution and linker substitution. The work discussed in this report emphasizes that the mixed-linker approach, broadly used for rigid frameworks, but only recently for flexible systems, provides a route to significant derivation of known flexible frameworks, enabling synthesis of systematically varied families of frameworks that may be used for more controlled studies (Table S2). If combined with *in situ* crystallographic measurements and modern computational approaches, this synthetic approach may enable rigorous investigations with unambiguous insights, dramatically improving our understanding of cooperative flexibility and step-shaped adsorption–desorption, leading to advancements in design, utility, and application. Indeed, the pressing goals of the field should be to achieve *de novo* and targeted design, as well as enabling computationally driven database searches for specific applications.

ASSOCIATED CONTENT

Supporting Information

The Supporting Information is available free of charge at:

Crystallographic figures; PXRD patterns; Proton NMR spectroscopy data; Fourier Transform Infrared (FTIR) spectroscopy data; Energy Dispersive X-Ray (EDX) analysis data; Thermal analysis data; Different gas adsorption–desorption data, and Computational analysis (PDF)

AUTHOR INFORMATION

Corresponding Author

C. Michael McGuirk – Department of Chemistry, Colorado School of Mines, Golden, Colorado 80401, United States; orcid.org/0000-0002-7420-1169; Email: cmmcguirk@mines.edu.

Author

Arijit Halder – Department of Chemistry, Colorado School of Mines, Golden, Colorado 80401, United States; <https://orcid.org/0000-0002-4047-2593>.

Notes

The authors declare no competing financial interest.

ACKNOWLEDGMENTS

A.H. and C.M.M. are thankful for the support from the US DOE EERE HFTO under Award Number DE-EE0008823 and from Colorado School of Mines in the form of start-up funding. The authors are thankful to Michael P. Moghadasnia of the Department of Chemistry, Colorado School of Mines, for his assistance with computational studies and fruitful discussions.

References:

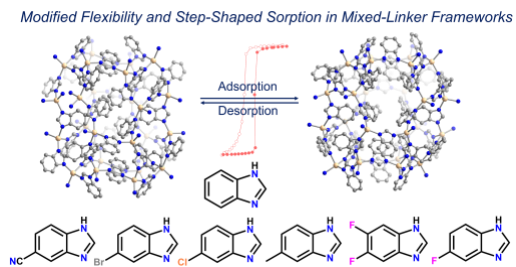
(1) Zhou, H.-C.; Long, J. R.; Yaghi, O. M. Introduction to Metal–Organic Frameworks. *Chem. Rev.* **2012**, *112* (2), 673-674, DOI: 10.1021/cr300014x.

- (2) Zhao, D.; Timmons, D. J.; Yuan, D.; Zhou, H.-C. Tuning the Topology and Functionality of Metal–Organic Frameworks by Ligand Design. *Acc. Chem. Res.* **2011**, *44* (2), 123-133, DOI: 10.1021/ar100112y.
- (3) Banerjee, R.; Phan, A.; Wang, B.; Knobler, C.; Furukawa, H.; O'Keeffe, M.; Yaghi, O. M. High-throughput synthesis of zeolitic imidazolate frameworks and application to CO₂ capture. *Science* **2008**, *319* (5865), 939-943, DOI: 10.1126/science.1152516.
- (4) Connolly, B. M.; Aragoñes-Anglada, M.; Gandara-Loe, J.; Danaf, N. A.; Lamb, D. C.; Mehta, J. P.; Vulpe, D.; Wuttke, S.; Silvestre-Albero, J.; Moghadam, P. Z.; et al. Tuning porosity in macroscopic monolithic metal-organic frameworks for exceptional natural gas storage. *Nat. Commun.* **2019**, *10* (1), 2345, DOI: 10.1038/s41467-019-10185-1.
- (5) Lyndon, R.; You, W.; Ma, Y.; Bacsá, J.; Gong, Y.; Stangland, E. E.; Walton, K. S.; Sholl, D. S.; Lively, R. P. Tuning the Structures of Metal–Organic Frameworks *via* a Mixed-Linker Strategy for Ethylene/Ethane Kinetic Separation. *Chem. Mater.* **2020**, *32* (9), 3715-3722, DOI: 10.1021/acs.chemmater.9b04177.
- (6) Yang, L.; Qian, S.; Wang, X.; Cui, X.; Chen, B.; Xing, H. Energy-efficient separation alternatives: metal–organic frameworks and membranes for hydrocarbon separation. *Chem. Soc. Rev.* **2020**, *49* (15), 5359-5406, DOI: 10.1039/c9cs00756c.
- (7) Kreno, L. E.; Leong, K.; Farha, O. K.; Allendorf, M.; Van Duyne, R. P.; Hupp, J. T. Metal–Organic Framework Materials as Chemical Sensors. *Chem. Rev.* **2012**, *112* (2), 1105-1125, DOI: 10.1021/cr200324t.
- (8) Pascanu, V.; González Miera, G.; Inge, A. K.; Martín-Matute, B. Metal–Organic Frameworks as Catalysts for Organic Synthesis: A Critical Perspective. *J. Am. Chem. Soc.* **2019**, *141* (18), 7223-7234, DOI: 10.1021/jacs.9b00733.
- (9) Bavykina, A.; Kolobov, N.; Khan, I. S.; Bau, J. A.; Ramirez, A.; Gascon, J. Metal–Organic Frameworks in Heterogeneous Catalysis: Recent Progress, New Trends, and Future Perspectives. *Chem. Rev.* **2020**, *120* (16), 8468-8535, DOI: 10.1021/acs.chemrev.9b00685.
- (10) Chen, Y.; Li, P.; Zhou, J.; Buru, C. T.; Đorđević, L.; Li, P.; Zhang, X.; Cetin, M. M.; Stoddart, J. F.; Stupp, S. I.; et al. Integration of Enzymes and Photosensitizers in a Hierarchical Mesoporous Metal–Organic Framework for Light-Driven CO₂ Reduction. *J. Am. Chem. Soc.* **2020**, *142* (4), 1768-1773, DOI: 10.1021/jacs.9b12828.
- (11) Liu, L.; Du, S.; Guo, X.; Xiao, Y.; Yin, Z.; Yang, N.; Bao, Y.; Zhu, X.; Jin, S.; Feng, Z.; Zhang, F. Water-Stable Nickel Metal–Organic Framework Nanobelts for Cocatalyst-Free Photocatalytic Water Splitting to Produce Hydrogen. *J. Am. Chem. Soc.* **2022**, *144* (6), 2747-2754, DOI: 10.1021/jacs.1c12179.
- (12) Xie, L. S.; Skorupskii, G.; Dincă, M. Electrically Conductive Metal–Organic Frameworks. *Chem. Rev.* **2020**, *120* (16), 8536-8580, DOI: 10.1021/acs.chemrev.9b00766.
- (13) Meng, H.; Han, Y.; Zhou, C.; Jiang, Q.; Shi, X.; Zhan, C.; Zhang, R. Conductive Metal–Organic Frameworks: Design, Synthesis, and Applications. *Small Methods* **2020**, *4* (10), 2000396, DOI: 10.1002/smt.202000396.
- (14) Schneemann, A.; Bon, V.; Schwedler, I.; Senkowska, I.; Kaskel, S.; Fischer, R. A. Flexible metal-organic frameworks. *Chem. Soc. Rev.* **2014**, *43*, 6062-6096, DOI: 10.1039/c4cs00101j.
- (15) Horike, S.; Shimomura, S.; Kitagawa, S. Soft porous crystals. *Nat. Chem.* **2009**, *1* (9), 695-704, DOI: 10.1038/nchem.444.
- (16) Peralta, R. A.; Huxley, M. T.; Lyu, P.; Díaz-Ramírez, M. L.; Park, S. H.; Obeso, J. L.; Leyva, C.; Heo, C. Y.; Jang, S.; Kwak, J. H.; et al. Engineering Catalysis within a Saturated

- In(III)-Based MOF Possessing Dynamic Ligand–Metal Bonding. *ACS Appl. Mater. Interfaces* **2023**, *15* (1), 1410-1417, DOI: 10.1021/acscami.2c19984.
- (17) Andreeva, A. B.; Le, K. N.; Chen, L.; Kellman, M. E.; Hendon, C. H.; Brozek, C. K. Soft Mode Metal-Linker Dynamics in Carboxylate MOFs Evidenced by Variable-Temperature Infrared Spectroscopy. *J. Am. Chem. Soc.* **2020**, *142* (45), 19291-19299, DOI: 10.1021/jacs.0c09499.
- (18) Obeso, J. L.; Huxley, M. T.; Leyva, C.; Gabriel Flores, J.; Martín-Guaregua, N.; Viniegra, M.; Aguilar-Pliego, J.; Antonio de los Reyes, J.; Ibarra, I. A.; Peralta, R. A. The role of dynamic metal-ligand bonds in metal-organic framework chemistry. *Coord. Chem. Rev.* **2023**, *496*, 215403, DOI: 10.1016/j.ccr.2023.215403.
- (19) Park, S. H.; Peralta, R. A.; Moon, D.; Jeong, N. C. Dynamic weak coordination bonding of chlorocarbons enhances the catalytic performance of a metal–organic framework material. *J. Mater. Chem. A* **2022**, *10* (44), 23499-23508, DOI: 10.1039/d2ta06208a.
- (20) Senkovska, I.; Bon, V.; Abylgazina, L.; Mendt, M.; Berger, J.; Kieslich, G.; Petkov, P.; Luiz Fiorio, J.; Joswig, J. O.; Heine, T.; et al. Understanding MOF Flexibility: An Analysis Focused on Pillared Layer MOFs as a Model System. *Angew. Chem., Int. Ed.* **2023**, *62* (33), e202218076, DOI: 10.1002/anie.202218076.
- (21) Miura, H.; Bon, V.; Senkovska, I.; Ehrling, S.; Watanabe, S.; Ohba, M.; Kaskel, S. Tuning the gate-opening pressure and particle size distribution of the switchable metal-organic framework DUT-8(Ni) by controlled nucleation in a micromixer. *Dalton Trans.* **2017**, *46*, 14002-14011, DOI: 10.1039/c7dt02809a.
- (22) Dybtsev, D. N.; Chun, H.; Kim, K. Rigid and Flexible: A Highly Porous Metal–Organic Framework with Unusual Guest-Dependent Dynamic Behavior. *Angew. Chem., Int. Ed.* **2004**, *43* (38), 5033-5036, DOI: 10.1002/anie.200460712.
- (23) Evans, J. D.; Bon, V.; Senkovska, I.; Lee, H.-C.; Kaskel, S. Four-dimensional metal-organic frameworks. *Nat. Commun.* **2020**, *11* (1), DOI: 10.1038/s41467-020-16527-8.
- (24) Thommes, M.; Kaneko, K.; Neimark, A. V.; Olivier, J. P.; Rodriguez-Reinoso, F.; Rouquerol, J.; Sing, K. S. W. Physisorption of gases, with special reference to the evaluation of surface area and pore size distribution (IUPAC Technical Report). *Pure Appl. Chem.* **2015**, *87* (9-10), 1051-1069, DOI: doi:10.1515/pac-2014-1117.
- (25) Halder, A.; Klein, R. A.; Shulda, S.; McCarver, G. A.; Parilla, P. A.; Furukawa, H.; Brown, C. M.; McGuirk, C. M. Multivariate Flexible Framework with High Usable Hydrogen Capacity in a Reduced Pressure Swing Process. *J. Am. Chem. Soc.* **2023**, *145*, 8042, DOI: 10.1021/jacs.3c00344.
- (26) Mason, J. A.; Oktawiec, J.; Taylor, M. K.; Hudson, M. R.; Rodriguez, J.; Bachman, J. E.; Gonzalez, M. I.; Cervellino, A.; Guagliardi, A.; Brown, C. M.; et al. Methane storage in flexible metal–organic frameworks with intrinsic thermal management. *Nature* **2015**, *527* (7578), 357-361, DOI: 10.1038/nature15732.
- (27) Madden, D. G.; O’Nolan, D.; Rampal, N.; Babu, R.; Çamur, C.; Al Shakhs, A. N.; Zhang, S. Y.; Rance, G. A.; Perez, J.; Maria Casati, N. P.; et al. Densified HKUST-1 Monoliths as a Route to High Volumetric and Gravimetric Hydrogen Storage Capacity. *J. Am. Chem. Soc.* **2022**, *144*, 13729-13739, DOI: 10.1021/jacs.2c04608.
- (28) Lawson, H. D.; Walton, S. P.; Chan, C. Metal–Organic Frameworks for Drug Delivery: A Design Perspective. *ACS Appl. Mater. Interfaces* **2021**, *13* (6), 7004-7020, DOI: 10.1021/acscami.1c01089.

- (29) Yuan, S.; Feng, L.; Wang, K.; Pang, J.; Bosch, M.; Lollar, C.; Sun, Y.; Qin, J.; Yang, X.; Zhang, P.; et al. Stable Metal–Organic Frameworks: Design, Synthesis, and Applications. *Adv. Mater.* **2018**, *30* (37), 1704303, DOI: 10.1002/adma.201704303.
- (30) Taylor, M. K.; Runčevski, T.; Oktawiec, J.; Gonzalez, M. I.; Siegelman, R. L.; Mason, J. A.; Ye, J.; Brown, C. M.; Long, J. R. Tuning the Adsorption-Induced Phase Change in the Flexible Metal–Organic Framework Co(bdp). *J. Am. Chem. Soc.* **2016**, *138* (45), 15019-15026, DOI: 10.1021/jacs.6b09155.
- (31) Roztocki, K.; Formalik, F.; Bon, V.; Krawczuk, A.; Goszczycki, P.; Kuchta, B.; Kaskel, S.; Matoga, D. Tuning Adsorption-Induced Responsiveness of a Flexible Metal–Organic Framework JUK-8 by Linker Halogenation. *Chem. Mater.* **2022**, *34* (7), 3430-3439, DOI: 10.1021/acs.chemmater.2c00249.
- (32) Henke, S.; Schneemann, A.; Wütscher, A.; Fischer, R. A. Directing the Breathing Behavior of Pillared-Layered Metal–Organic Frameworks via a Systematic Library of Functionalized Linkers Bearing Flexible Substituents. *J. Am. Chem. Soc.* **2012**, *134* (22), 9464-9474, DOI: 10.1021/ja302991b.
- (33) Klein, R. A.; Shulda, S.; Parilla, P. A.; Le Magueres, P.; Richardson, R. K.; Morris, W.; Brown, C. M.; McQuirk, C. M. Structural resolution and mechanistic insight into hydrogen adsorption in flexible ZIF-7. *Chem. Sci.* **2021**, *12*, 15620-15631, DOI: 10.1039/D1SC04618G.
- (34) McQuirk, C. M.; Runčevski, T.; Oktawiec, J.; Turkiewicz, A.; Taylor, M. K.; Long, J. R. Influence of Metal Substitution on the Pressure-Induced Phase Change in Flexible Zeolitic Imidazolate Frameworks. *J. Am. Chem. Soc.* **2018**, *140*, 15924-15933, DOI: 10.1021/jacs.8b09631.
- (35) Helal, A.; Yamani, Z. H.; Cordova, K. E.; Yaghi, O. M. Multivariate metal-organic frameworks. *Natl. Sci. Rev.* **2017**, *4* (3), 296-298, DOI: 10.1093/nsr/nwx013.
- (36) Halder, A.; Klein, R. A.; Lively, R.; McQuirk, C. M. Multivariate zeolitic imidazolate frameworks with an inverting trend in flexibility. *Chem. Commun.* **2022**, *58*, 11394-11397, DOI: 10.1039/D2CC04362A.
- (37) Klein, R. A.; Bingel, L. W.; Halder, A.; Carter, M.; Trump, B. A.; Bloch, E. D.; Zhou, W.; Walton, K. S.; Brown, C. M.; McQuirk, C. M. Adaptive Pore Opening to Form Tailored Adsorption Sites in a Cooperatively Flexible Framework Enables Record Inverse Propane/Propylene Separation. *J. Am. Chem. Soc.* **2023**, *145* (40), 21955-21965, DOI: 10.1021/jacs.3c06754.
- (38) Zhao, P.; Fang, H.; Mukhopadhyay, S.; Li, A.; Rudić, S.; McPherson, I. J.; Tang, C. C.; Fairen-Jimenez, D.; Tsang, S. C. E.; Redfern, S. A. T. Structural dynamics of a metal–organic framework induced by CO₂ migration in its non-uniform porous structure. *Nat. Commun.* **2019**, *10* (1), 999, DOI: 10.1038/s41467-019-08939-y.
- (39) Du, Y.; Wooller, B.; Nines, M.; Kortunov, P.; Paur, C. S.; Zengel, J.; Weston, S. C.; Ravikovitch, P. I. New High- and Low-Temperature Phase Changes of ZIF-7: Elucidation and Prediction of the Thermodynamics of Transitions. *J. Am. Chem. Soc.* **2015**, *137* (42), 13603-13611, DOI: 10.1021/jacs.5b08362.
- (40) Choi, H. J.; Dincă, M.; Long, J. R. Broadly Hysteretic H₂ Adsorption in the Microporous Metal–Organic Framework Co(1,4-benzenedipyrazolate). *J. Am. Chem. Soc.* **2008**, *130* (25), 7848-7850, DOI: 10.1021/ja8024092.

For Table of Contents Use Only



The mixed-linker approach in cooperatively flexible metal–organic frameworks unlock a diverse library of functionally modified structures, providing insights into influential electronic variables. This methodology simultaneously expands the range of applicable materials while enhancing understanding of their electronic characteristics for specific applications.